Transition Path Dynamics of a Dielectric Particle in a Bistable Optical Trap

Niels Zijlstra,[1,*,†] Daniel Nettels,[1,‡] Rohit Satija,[2] Dmitrii E. Makarov,[2,§] and Benjamin Schuler[1,3,‖]
[1]Department of Biochemistry, University of Zurich, 8057 Zurich, Switzerland
[2]Department of Chemistry and Oden Institute for Computational Engineering and Sciences, University of Texas at Austin, Austin, Texas 78712, USA
[3]Department of Physics, University of Zurich, 8057 Zurich, Switzerland

(Received 2 February 2020; accepted 28 August 2020; published 28 September 2020)

Many processes in chemistry, physics, and biology involve rare events in which the system escapes from a metastable state by surmounting an activation barrier. Examples range from chemical reactions, protein folding, and nucleation events to the catastrophic failure of bridges. A challenge in understanding the underlying mechanisms is that the most interesting information is contained within the rare transition paths, the exceedingly short periods when the barrier is crossed. To establish a model process that enables access to all relevant timescales, although highly disparate, we probe the dynamics of single dielectric particles in a bistable optical trap in solution. Precise localization by high-speed tracking enables us to resolve the transition paths and relate them to the detailed properties of the 3D potential within which the particle diffuses. By varying the barrier height and shape, the experiments provide a stringent benchmark of current theories of transition path dynamics.

DOI: 10.1103/PhysRevLett.125.146001

Rate processes in which a system escapes from metastable states via an activation barrier take place on timescales that are long compared to the relaxation dynamics within the states. This separation of timescales allows for the interconversion between states to be approximated in terms of phenomenological chemical kinetics by employing a set of rate coefficients and effectively assuming that the actual interconversion between states is instantaneous [1]. For microscopic systems, a Kramers-type description of the underlying dynamics is more realistic, where the rate coefficients are related to the diffusive motion on an energy surface [2]. This concept has been successfully applied to complex processes such as protein folding and binding [3–5] and provides a conceptual link between the phenomenological kinetics and the underlying molecular dynamics, including the actual process of barrier crossing. These transition paths (TPs) across the barrier contain the most interesting information about the mechanism of the reaction [6], and their investigation has made great progress in the past ten years owing to advances in single-molecule experiments and the concomitant development of theoretical concepts [3,6–15].

Experimental limitations and the complexity of biomolecular systems, however, pose considerable challenges. For instance, the microsecond timescale of typical biomolecular TPs seriously limits the amount of information accessible with experimental time resolution; the choice of reaction coordinates is constrained by the experimentally accessible observables; the actual underlying potentials are often unknown; and data analysis thus requires simplifying assumptions regarding the shape of the energy surface and the nature of the dynamics. To complement the ongoing efforts to overcome such difficulties, our goal here is to provide a simple experimental system that enables all relevant parameters to be extracted directly from the measurements; that covers a broad range of timescales to enable both extensive sampling of the rare transitions and the necessary time resolution to fully resolve TPs; and that allows the shape of the potential to be tuned systematically. Such a system would enable a stringent comparison to simulations and a rigorous test of theoretical concepts at a level of detail that has previously been inaccessible.

To achieve this goal, we employ a spherical dielectric Brownian particle trapped in an optical double-well potential [Fig. 1(a), Supplemental Material [16], Fig. 1]. This configuration has previously been used to test Kramers' theory, e.g., the calculation of rate coefficients based on the shape of the potential [21], the dependence of rates on the damping regime [22], and the transition between ballistic and diffusive motion [23]. The approach is also ideally suited for investigating TPs between the two traps. High-speed camera-based tracking [24–26] enables 3D localization with microsecond time resolution combined with hour-long recording times (Fig. 1, Supplemental Material [16], Fig. 2). The data thus provide both the requisite statistics for obtaining precise transition rates from individual trajectories and the ability to resolve the millisecond TPs [Fig. 1(e)]. Particle position trajectories show the expected bistability of the system in time [Fig. 1(b)]; position autocorrelation functions [Fig. 1(c)] illustrate the eight orders of magnitude accessible in time and reveal both the diffusive dynamics within the traps and the

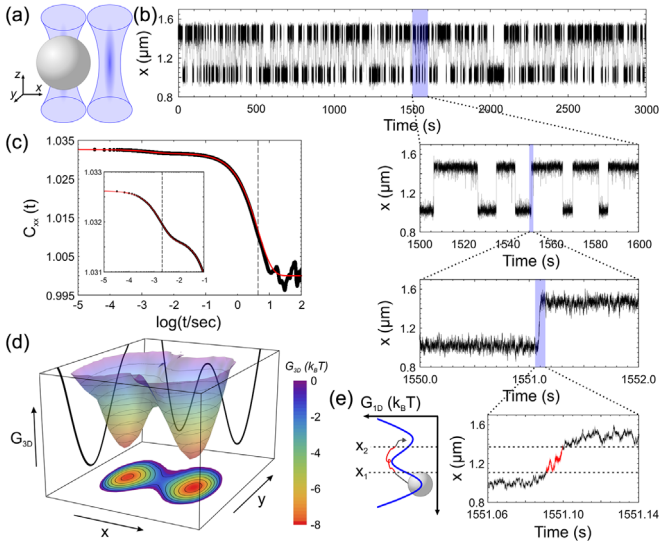

FIG. 1. Transition paths in the bistable optical trap. (a) Schematic of a microsphere (fused silica, radius ∼270 nm) in a bistable trap formed by two laser foci (wavelength 485 nm) separated by ∼450 nm. The z coordinate is deduced from the ring pattern of the diffraction-limited image of the bead with a precision of ∼50 nm; its symmetry center yields the x and y coordinates with a precision of ∼25 nm. See the Supplemental Material [16] for technical details. (b) A trajectory along x, the interfocus axis, with enlargements at increasing time resolutions. (c) The position autocorrelation function C_{xx} reveals diffusive dynamics within the traps (correlation time 2.2 ± 0.1 ms) and kinetics of transitions between them ($k^{-1} = 4.4 \pm 0.1$ s). The red line is a fit with $C_{xx}(t) = \langle x \rangle^2 e^{-kt} + (k_B T/\kappa) e^{-(D\kappa/k_B T)t} + 1$, where $\langle x \rangle$ is the trap separation, k the transition rate between the wells, κ the average curvature of the free energy at the bottom of the two wells, and D the diffusion constant. (d) The 3D potential, G_{3D}, extracted from the distribution of the particle positions (color projection). (e) Illustration of a TP (red) between boundaries x_1 and x_2 along the one-dimensional free-energy profile, $G_{1D}(x)$ (duration in this example 8.8 ms).

kinetics of transitions between them. From the distribution $P_{3D}(\mathbf{r})$ of the particle's position $\mathbf{r} = (x, y, z)$ based on 10^6 to 10^8 images per trajectory, the three-dimensional free-energy landscape is readily reconstructed as $G_{3D}(\mathbf{r}) = -k_B T \ln P_{3D}(\mathbf{r})$, where k_B is Boltzmann's constant and T is temperature [Fig. 1(d)]. The diffusion coefficient D of each particle was determined from its mean-squared displacement at short times [21] (Supplemental Material [16], Fig. 3). Notably, variations in particle shape and size lead to variations by ∼10% in D; similarly, such particle-to-particle variations and the possible influence of Mie resonances [27] at a given shape and radiant flux of the laser beams lead to clearly detectable differences in the shapes of the potentials (Supplemental Material [16], Figs. 3 and 4). However, since the potentials are obtained by Boltzmann inversion for each particle and laser power individually, all these contributions are accounted for and do not need to be modeled explicitly. By adjusting the

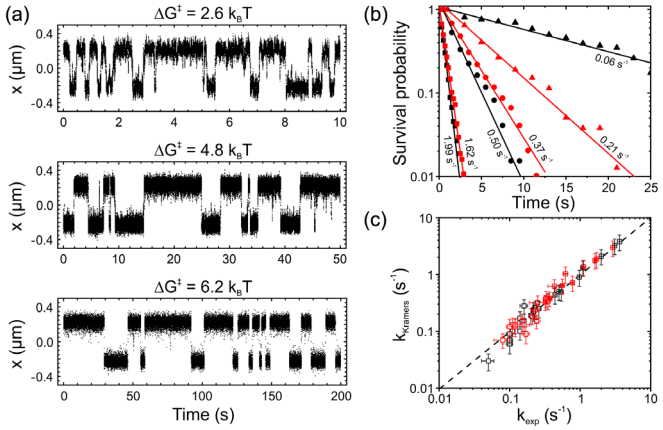

FIG. 2. Transition rates and Kramers' theory. (a) Examples of particle trajectories projected on the interfocus axis x [cf. Fig. 1 (a)] with different barrier heights and transition frequencies. (b) Survival probability distributions in the traps fitted with exponential decays (lines) yield the interwell transition rate coefficients. Since the potentials are never perfectly symmetric, transitions in the two directions are analyzed separately (black: x increasing; red: x decreasing, identical symbols: same particle). (c) Comparison of the transition rate coefficients according to Kramers' theory, k_{Kramers}, with measured values, k_{exp} (black: x increasing; red: x decreasing; identity line: dashed). Error bars for k_{Kramers} result from uncertainties in the barrier and well curvatures and barrier heights, error bars in k_{exp} from uncertainties in the fits of the survival probability distributions (b).

laser power, we can tune the barrier height systematically between ∼2 and 8 $k_B T$, corresponding to a hundredfold change in transition rate coefficients (Fig. 2). The accessible range of rates is limited at low laser power by the loss of persistent trapping, and at high laser power by insufficient sampling of the potential in the transition region.

As the friction force on the particle obeys Stokes' law and is proportional to its velocity, we expect the particle dynamics to be described by a three-dimensional Langevin equation in the potential $G_{3D}(\mathbf{r})$. Since the particle's motion is overdamped [21,22], inertial contributions can be neglected [2]. The kinetics of transitions between the wells can then be described using Langer's rate theory of multidimensional diffusive barrier crossing [28]. The symmetry of the potential suggests that the reaction coordinate of this process coincides with the x axis along the interfocus distance (Fig. 1); moreover, because of the symmetry of the potential at stationary points, the dynamics along x are decoupled from those along y and z near the barrier saddle. As a result, Kramers model [29] of one-dimensional diffusive barrier crossing in the 1D free-energy landscape $G_{1D}(x) = -k_B T \ln P_{1D}(x)$ is sufficient, where $P_{1D}(x) = \iint P_{3D}(\mathbf{r}) dy dz$ is the probability distribution of the position along x. The Kramers rate for crossing a barrier of height $\Delta G^{\ddagger}$ is

$$k_{\mathrm{Kramers}} = (D\sqrt{\kappa_b \kappa_w}/2\pi) e^{-\Delta G^{\ddagger}/k_B T}, \qquad (1)$$

where κ_b and κ_w are the curvatures of the potential $G_{1D}(x)$ at the top of its barrier and at the bottom of the initial potential well, respectively. Note that D is independent of position in our experimental system. To test the applicability of the Kramers' theory, we extracted transition rate coefficients from the measured particle trajectories projected on x, assuming first-order kinetics between the two states, and compared them to the values from a Kramers model (Fig. 2), using $G_{1D}(x)$ (Supplemental Material [16], Fig. 5) and D obtained for the respective individual particles from their mean-square displacements after short times (see the Supplemental Material [16]). The agreement [Fig. 2(c)] confirms the applicability of Kramers' theory [21] and illustrates the high data quality available from individual particle trajectories.

Examples of transitions from one trap to the other are shown in Fig. 3(a), projected on the xy and xz planes, and along x. TPs are the segments of the trajectory where the particle continuously dwells in the transition region between the two potential wells, having entered it from one well and exiting to the other [red segments in Fig. 3(a)]. For trajectories in 3D, we defined the boundaries of the transition regions as isoenergetic surfaces enclosing the potential minima, $G_{3D}(\mathbf{r}) = E_1$ and $G_{3D}(\mathbf{r}) = E_2$, where E_1 and E_2 were chosen as the energy values halfway between the barrier top and the bottom of the respective minima of the potential, $G_{3D}(x, \langle y \rangle, \langle z \rangle)$. For 1D projections, $x(t)$, the boundaries correspond to the values x_1 and x_2 defined by $G_{1D}(x) = E_1$ and $G_{1D}(x) = E_2$, with E_1 and E_2 chosen halfway between the barrier top and the respective minima of $G_{1D}(x)$. The transition region then coincides with the interval $[x_1, x_2]$. Although the TPs identified in 3D differ from those identified in 1D or 2D, the mean TP times in 1D are on average only ~15% shorter than in 3D, indicating robustness to the dimensionality of the analysis used (Supplemental Material [16], Fig. 6).

The average TP times $\langle \tau_{\mathrm{TP}} \rangle$ are well reproduced by Brownian dynamics simulations in the corresponding potentials, over a wide range of barrier heights and for different choices of TP boundaries [Fig. 3(b)]. The agreement is similarly good for the numerical solution of the diffusion problem using the detailed shapes of the potentials [31]. Remarkably, $\langle \tau_{\mathrm{TP}} \rangle$ for all but the lowest barriers are almost as well reproduced by the Szabo approximation [3,6,30], according to which $\langle \tau_{\mathrm{TP}} \rangle = (k_B T / D\kappa_b) \ln(2e^{\gamma} \Delta G^* / k_B T)$, where ΔG^* is the barrier height measured relative to the values of $G_{1D}(x)$ at the TP boundaries, and $\gamma \approx 0.577$ is Euler's constant. This relation, derived for diffusive crossing of a symmetric parabolic 1D barrier with $\Delta G^* \gg k_B T$ [30], is commonly used for the analysis of experimentally measured biomolecular TP times [6,10], where information about the shape of the potential is often unavailable. Figure 3(c) illustrates an important observation: in contrast to the transition rates, which depend exponentially on the activation free energy [Eq. (1), Fig. 2(c)], TP times are much

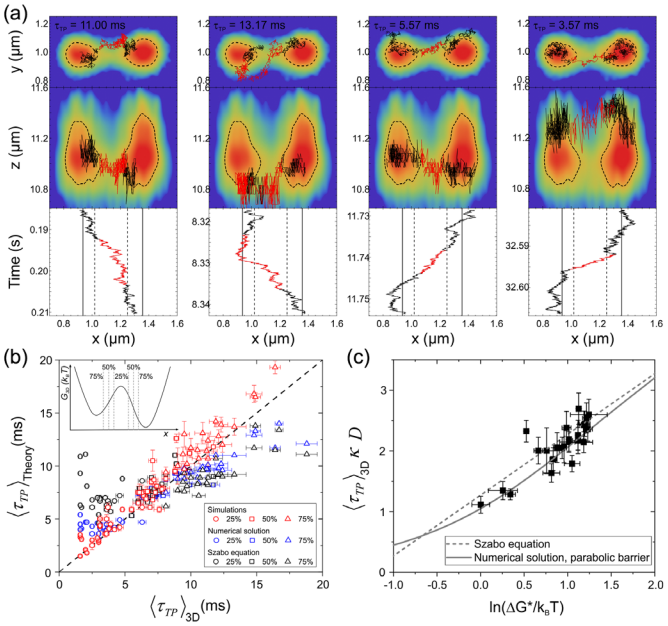

FIG. 3. Quantifying TP times and dependence on barrier height. (a) Examples of TPs projected on the xy and xz planes (top), with the free energy shown by the color scale as in Fig. 1. Dashed lines indicate the TP boundary in the xy and xz planes; red trajectory segments indicate the TPs identified in 3D. The bottom panels show the TPs projected onto the x axis. Solid vertical lines indicate trap centers, dashed lines TP boundaries along x. (b) Measured average TP times for each particle compared to the results from 3D-Brownian dynamics simulations (red symbols), to the numerical solution of the 1D diffusion problem on the measured potential of mean force (blue symbols), and to the results from theory using the Szabo equation [3,6,30] (black symbols, averages of ΔG^* in both directions of the transition were used) with different TP boundaries (see inset and legend). (c) Average TP times for each particle using TP boundaries at 50% [see inset in (b)] compared with the Szabo approximation (gray dashed line) and the numerical solution (solid gray line) using the curvatures of the experimentally determined potentials and the diffusion coefficient averaged over all measurements.

less sensitive to the barrier height. The dependence of $\langle \tau_{\mathrm{TP}} \rangle$ on ΔG^* is also well described by the Szabo equation.

The time resolution of our experiment allows us to quantify not only average TP times but also their distributions and the dependence on the barrier height for each particle (Fig. 4 and Supplemental Material [16], Fig. 7). As expected for diffusive barrier crossing, we observe peaked asymmetric distributions with exponential tails [31,32]. The distributions are compared with those predicted by three theoretical models: Brownian dynamics simulations using $G_{3D}(\mathbf{r})$ and D from the experiments; the numerical solution for diffusive dynamics in $G_{1D}(x)$ [31]; and the analytical approximation for the diffusive dynamics across a high 1D parabolic barrier [32]. All three approaches are in remarkably good agreement with experiment for barriers with $\Delta G^* > 3k_b T$ [Fig. 4(a)]. For smaller barriers, the analytical approximation deviates from the experimental

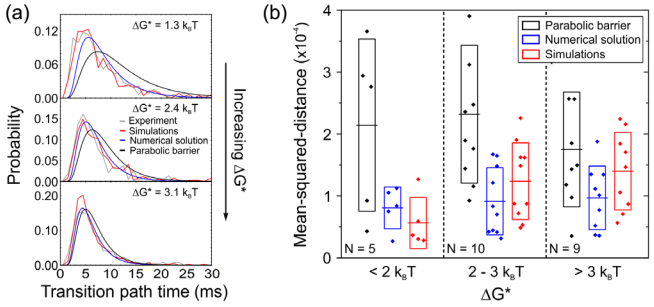

FIG. 4. Transition path time distributions for different barrier heights. (a) Examples of TP time distributions from measurements of individual particles (barrier heights given in each panel). Experimentally determined distributions (gray) are compared to 3D Brownian dynamics simulations (red), the numerical solution for 1D diffusion in the potential (blue) [31], and the analytical approximation for a parabolic barrier (black) [32]. (b) Mean-squared-distance (χ^2) between experimental and theoretical TP time distributions, divided into low ($\Delta G^* < 2k_bT$), intermediate ($2k_bT < \Delta G^* < 3k_bT$), and high ($\Delta G^* > 3k_bT$) barrier heights ΔG^* (averaged in both directions). (Symbols: individual measurements; solid line: average; rectangles: standard deviation of mean-squared-distance; N: number of distributions, each from an individual particle, contributing to each class.)

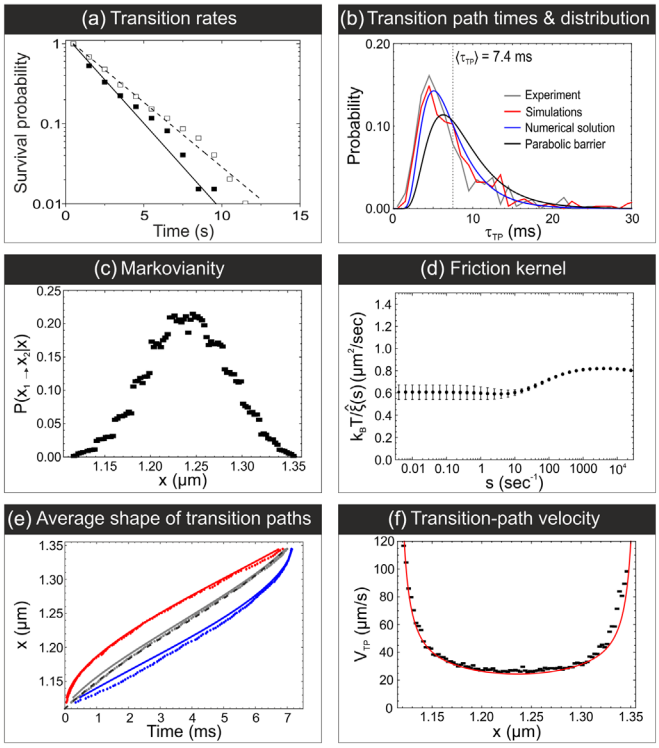

FIG. 5. Detailed information on transition paths. The dynamics of dielectric particles in a bistable optical trap provides a wide range of information and direct comparison to theory, including (a) transition rates from dwell-time distributions, (b) distributions of TP times, (c) the Markovianity of the process [33], (d) the friction memory kernel [Eq. (10) in Ref. [34]], (e) the average shape of the TPs (circles: experiment, lines: theory; red and blue: average first and last crossing times [35], gray: average TP shape [Eq. (4) in Ref. [36]]. Interestingly, the average TP is nearly indistinguishable from the most probable TP [37] estimated using the harmonic approximation [Eq. (6) in Ref. [38]], dashed black line. (f) The transition-path velocity as defined in Ref. [39] [Eq. (5)] (black symbols) compared with the theoretical prediction [red line, Eq. (17) in Ref. [39]]. See main text and the Supplemental Material [16] for details and equations.

data, whereas 3D simulations and the 1D numerical solution agree to within error down to very low barriers.

The TP time is an important property, but much more information can be gleaned from the observed barrier crossing dynamics. For instance, most of the analyses of TP times in single-molecule experiments have relied on the *a priori* assumption of diffusive dynamics. However, this assumption (which does not necessarily hold for molecular reaction coordinates) can be tested directly here: first, we applied the recently proposed Markovianity test [33], which computes the conditional probability $P(x_1 \to x_2|x)$ that the system at point x (with $x_1 < x < x_2$) is on a TP from boundary x_1 to boundary x_2. For a Markov process, this probability peaks at a value of 0.25, whereas memory effects reduce its maximum value. In our experiments, the observed barrier crossing dynamics indeed closely approach Markovianity [Fig. 5(c)]. The residual deviation from 0.25 is presumably caused by the rare misidentification of fast TPs (Supplemental Material [16], Fig. 11).

Second, we applied a more general dynamic model to the observed $x(t)$ in which the friction force is not simply proportional to the instantaneous velocity $\dot{x}(t)$ but depends on past velocities, $F_{\rm fr} = -\int_{-\infty}^{t} \xi(t-t')\dot{x}(t')dt'$. The friction memory kernel, $\xi(t)$, can be reconstructed directly from the observed trajectories [34]. The Laplace transform of $\xi(t)$, $\hat{\xi}(s) = \int_0^\infty \xi(t)e^{-st}dt$, is close to a constant, $\hat{\xi}(s) = \xi_0$, in the experimentally accessible frequency range [Fig. 5(d)], which means that $\xi(t)$ is well approximated by a delta function, and $F_{\rm fr}$ is simply proportional to the instantaneous velocity, $F_{\rm fr} = -\xi_0\dot{x}$, providing direct evidence for diffusive dynamics. Moreover, the resulting estimate of D based on the Einstein relation, $D = k_BT/\xi_0$, agrees with the values from the mean square displacement and the position correlation function (Supplemental Material [16], Fig. 3).

Finally, we quantified the average shape of the TPs [35,36,38] [Fig. 5(e)] and the transition-path velocity profile [33], $v_{\rm TP}(x)$ [Fig. 5(f)], which characterizes the dynamics of barrier crossing in terms of the time derivative of the average shape. Consistent with the model of diffusive crossing of a parabolic barrier, these profiles are monotonic functions of the coordinate with a minimum at the barrier top [35,38,39].

In summary, high-speed tracking of dielectric particles in a bistable optical trap thus provides the opportunity to resolve TPs of a diffusive barrier crossing process with great precision and to quantify their properties in unprecedented detail. A key strength of the approach is that the parameters determining the dynamics—the 3D shape of the

potential and the diffusion coefficient of the particle—can be extracted directly from the experimental data, essentially without simplifying assumptions. The results thus offer a stringent experimental benchmark for the theoretical concepts used in the investigation of TPs [3,6–14]. Given that applying a broad range of analysis tools to our experimental model system allowed us to correctly recover details of its underlying dynamics without making any prior assumptions regarding, e.g., the validity of the Kramers picture, our results are very encouraging for the field of single-molecule biophysics, as we expect that the same approach can be used to infer accurate models of barrier crossing dynamics directly from biomolecular transition paths. Experiments of this type and their analysis may help to address challenging open questions regarding TPs, such as the discrepancy between barrier heights using different types of analysis [9], or the observation of TP velocity profiles with a maximum instead of a minimum [40].

We thank Attila Szabo for many valuable discussions and comments on the manuscript. This work was supported by the Swiss National Science Foundation (to B. S.), by the Forschungskredit of the University of Zurich (to N. Z.), by the Robert W. Welch Foundation (Grant No. F-1514 to D. E. M.) and by the U.S. National Science Foundation (Grant No. CHE 1566001 to D. E. M.).

*Present address: Physical and Synthetic Biology, Faculty of Biology, Ludwig-Maximilans-Universität München, Großhadernerstrasse 2-4, 82152 Planegg-Martinsried, Germany
†n.zijlstra@lmu.de
‡nettels@bioc.uzh.ch
§makarov@cm.utexas.edu
‖schuler@bioc.uzh.ch

[1] N. G. van Kampen, *Stochastic Processes in Physics and Chemistry* (Elsevier, New York, 1992).
[2] P. Hänggi, P. Talkner, and M. Borkovec, Reaction-rate theory: fifty years after Kramers, Rev. Mod. Phys. **62**, 251 (1990).
[3] H. S. Chung, J. M. Louis, and W. A. Eaton, Experimental determination of upper bound for transition path times in protein folding from single-molecule photon-by-photon trajectories, Proc. Natl. Acad. Sci. U.S.A. **106**, 11837 (2009).
[4] D. Shoup and A. Szabo, Role of diffusion in ligand binding to macromolecules and cell-bound receptors, Biophys. J. **40**, 33 (1982).
[5] R. B. Best and G. Hummer, Diffusion models of protein folding, Phys. Chem. Chem. Phys. **13**, 16902 (2011).
[6] G. Hummer, From transition paths to transition states and rate coefficients, J. Chem. Phys. **120**, 516 (2004).
[7] P. G. Bolhuis, D. Chandler, C. Dellago, and P. L. Geissler, Transition path sampling: Throwing ropes over rough mountain passes, in the dark, Annu. Rev. Phys. Chem. **53**, 291 (2002).
[8] D. E. Makarov, *Single Molecule Science: Physical Principles and Models* (CRC Press, Boca Raton, 2015).
[9] K. Neupane, D. A. N. Foster, D. R. Dee, H. Yu, F. Wang, and M. T. Woodside, Direct observation of transition paths during the folding of proteins and nucleic acids, Science **352**, 239 (2016).
[10] H. S. Chung and W. A. Eaton, Protein folding transition path times from single molecule FRET, Curr. Opin. Struct. Biol. **48**, 30 (2018).
[11] R. B. Best and G. Hummer, Microscopic interpretation of folding phi-values using the transition path ensemble, Proc. Natl. Acad. Sci. U.S.A. **113**, 3263 (2016).
[12] K. Lindorff-Larsen, S. Piana, R. O. Dror, and D. E. Shaw, How fast-folding proteins fold, Science **334**, 517 (2011).
[13] F. Sturzenegger, F. Zosel, E. D. Holmstrom, K. J. Buholzer, D. E. Makarov, D. Nettels, and B. Schuler, Transition path times of coupled folding and binding reveal the formation of an encounter complex, Nat. Commun. **9**, 4708 (2018).
[14] N. Q. Hoffer and M. T. Woodside, Probing microscopic conformational dynamics in folding reactions by measuring transition paths, Curr. Opin. Chem. Biol. **53**, 68 (2019).
[15] E. Weinan and E. Vanden-Eijnden, Transition-path theory and path-finding algorithms for the study of rare events, Annu. Rev. Phys. Chem. **61**, 391 (2010).
[16] See the Supplemental Material at http://link.aps.org/supplemental/10.1103/PhysRevLett.125.146001 for methods and Supplemental Figures, which includes Refs. [17–20].
[17] A. Jain, A. H. Yang, and D. Erickson, Gel-based optical waveguides with live cell encapsulation and integrated microfluidics, Opt. Lett. **37**, 1472 (2012).
[18] A. Berezhkovskii and A. Szabo, One-dimensional reaction coordinates for diffusive activated rate processes in many dimensions, J. Chem. Phys. **122**, 014503 (2005).
[19] D. E. Makarov, Interplay of non-Markov and internal friction effects in the barrier crossing kinetics of biopolymers: Insights from an analytically solvable model, J. Chem. Phys. **138**, 014102 (2013).
[20] R. F. Grote and J. T. Hynes, The stable states picture of chemical reactions. II. Rate constants for condensed and gas phase reaction models, J. Chem. Phys. **73**, 2715 (1980).
[21] L. I. McCann, M. Dykman, and B. Golding, Thermally activated transitions in a bistable three-dimensional optical trap, Nature (London) **402**, 785 (1999).
[22] L. Rondin, J. Gieseler, F. Ricci, R. Quidant, C. Dellago, and L. Novotny, Direct measurement of Kramers turnover with a levitated nanoparticle, Nanotechnology **12**, 1130 (2017).
[23] T. Li, S. Kheifets, D. Medellin, and M. G. Raizen, Measurement of the instantaneous velocity of a Brownian particle, Science **328**, 1673 (2010).
[24] B. M. Lansdorp, S. J. Tabrizi, A. Dittmore, and O. A. Saleh, A high-speed magnetic tweezer beyond 10,000 frames per second, Rev. Sci. Instrum. **84**, 044301 (2013).
[25] A. Huhle, D. Klaue, H. Brutzer, P. Daldrop, S. Joo, O. Otto, U. F. Keyser, and R. Seidel, Camera-based three-dimensional real-time particle tracking at kHz rates and Ångstrm accuracy, Nat. Commun. **6**, 5885 (2015).
[26] R. Parthasarathy, Rapid, accurate particle tracking by calculation of radial symmetry centers, Nat. Methods **9**, 724 (2012).

[27] A. B. Stilgoe, T. A. Nieminen, G. Knöner, N. R. Heckenberg, and H. Rubinsztein-Dunlop, The effect of Mie resonances on trapping in optical tweezers, Opt. Express **16**, 15039 (2008).
[28] J. Langer, Statistical theory of the decay of metastable states, Ann. Phys. (N.Y.) **54**, 258 (1969).
[29] H. A. Kramers, Brownian motion in a field of force and the diffusion model of chemical reactions, Physica **7**, 284 (1940).
[30] H. S. Chung and I. V. Gopich, Fast single-molecule FRET spectroscopy: theory and experiment, Phys. Chem. Chem. Phys. **16**, 18644 (2014).
[31] S. Chaudhury and D. E. Makarov, A harmonic transition state approximation for the duration of reactive events in complex molecular rearrangements, J. Chem. Phys. **133**, 034118 (2010).
[32] B. W. Zhang, D. Jasnow, and D. M. Zuckerman, Transition-event durations in one-dimensional activated processes, J. Chem. Phys. **126**, 074504 (2007).
[33] A. M. Berezhkovskii and D. E. Makarov, Single-molecule test for Markovianity of the dynamics along a reaction coordinate, J. Phys. Chem. Lett. **9**, 2190 (2018).
[34] R. Satija and D. E. Makarov, Generalized Langevin equation as a model for barrier crossing dynamics in biomolecular folding, J. Phys. Chem. B **123**, 802 (2019).
[35] W. K. Kim and R. R. Netz, The mean shape of transition and first-passage paths, J. Chem. Phys. **143**, 224108 (2015).
[36] D. E. Makarov, Shapes of dominant transition paths from single-molecule force spectroscopy, J. Chem. Phys. **143**, 194103 (2015).
[37] P. Faccioli, M. Sega, F. Pederiva, and H. Orland, Dominant Pathways in Protein Folding, Phys. Rev. Lett. **97**, 108101 (2006).
[38] P. Cossio, G. Hummer, and A. Szabo, Transition paths in single-molecule force spectroscopy, J. Chem. Phys. **148**, 123309 (2018).
[39] A. M. Berezhkovskii and D. E. Makarov, Communication: Transition-path velocity as an experimental measure of barrier crossing dynamics, J. Chem. Phys. **148**, 201102 (2018).
[40] K. Neupane, N. Q. Hoffer, and M. T. Woodside, Measuring the Local Velocity along Transition Paths During the Folding of Single Biological Molecules, Phys. Rev. Lett. **121**, 018102 (2018).

Supplementary Information for:

Transition path dynamics of a dielectric particle in a bistable optical trap

Niels Zijlstra[1,4], Daniel Nettels[1], Rohit Satija[2], Dmitrii E. Makarov[2], Benjamin Schuler[1,3]

[1]Department of Biochemistry, University of Zurich, 8057 Zurich, Switzerland.

[2]Department of Chemistry and Oden Institute for Computational Engineering and Sciences, University of Texas at Austin, Austin, Texas 78712, USA.

[3]Department of Physics, University of Zurich, 8057 Zurich, Switzerland.

[4]Current address: Physical and Synthetic Biology, Faculty of Biology, Ludwig-Maximilians-Universität München, Großhadernerstrasse 2-4, 82152 Planegg-Martinsried, Germany

Methods

Instrumentation

Two optical traps were formed in an inverted microscope (Olympus IX-71) equipped with a water immersion objective (NA=1.2, 60x, PlanApo, Olympus) using a Nomarski prism and a linearly polarized laser beam from a continuous-wave solid state laser (λ = 485 nm, Sapphire 488-100 CDRH, Coherent) (Supplementary Figure 1). The relative intensities of the two traps were tuned by rotating a lambda-half plate positioned in the laser beam after a polarizer. Each of the two laser foci creates a stable three-dimensional potential well. The trap stiffness, and hence the depth of the potential wells, increases with increasing laser power. The distance between the two wells (~450 nm) is stably defined by the Nomarksi prism used. The sealed sample chamber, made from two glass cover slides separated by a polydimethylsiloxane spacer, contained a dilute solution of fused-silica microspheres (0.54 µm diameter, Bangs Laboratories) in water at room temperature. Using this configuration, we do not observe any drift in the position of a trapped microsphere over a duration of at least an hour (Supplementary Figure 2).

A single trapped particle was imaged with a high-speed CMOS camera (EoSens 4CXP CoaXPress, Mikrotron, Germany) using linearly polarized light from a 100-W mercury lamp using Köhler illumination. The camera was connected to a computer via a frame-grabber card (Active Silicon CoaXPress CXP-6 FireBird) and operated at 30,000 frames per second. Images were recorded directly to a high-speed SSD hard drive using the software StreamPix (NorPix inc., Canada). To achieve sufficiently high frame rates, the recorded region of interest was limited to 128 x 18 pixels, with a pixel size of 117 nm. To reduce the data throughput to a level compatible with the SSD write speed, 20 consecutive frames were read into the buffer of the frame grabber card and subsequently written on the SSD drive as a single frame. Before analyzing the movies, each frame was split into 20 individual frames using custom-written software in C++.

Particle localization

Before applying the localization routine, all frames were divided by a pre-recorded background image of the same area but without any particle present to reduce the influence of static camera noise. Subsequently, the coordinates of the center of the microsphere in the focal plane (xy) of the objective lens were found using an algorithm that determines the center of a radially symmetric pattern [1]. An accuracy of ~25 nm was achieved based on simulated particle images with comparable signal-to-noise as in the experiment. The coordinate in the direction of laser beam propagation (z) is extracted from the shape of the diffraction pattern of the particle image. For this purpose, we recorded calibration stacks using immobilized particles embedded in a 2% agarose gel (Supplementary Figures 8 and 9), which is ideally suited for this purpose since its refractive index is within ~0.02% of the value for water [2]. The z-position of the particle was controlled via a piezo-actuated nanopositioner (PIFOC, Physik Instrumente, Germany) and adjusted in 50-nm increments over a range of 9 to 12.5 µm. Each calibration image was an average of 10,000 frames recorded at 30 kHz frame rate. After determining the center of symmetry, we obtained a radial intensity profile by angular integration. Finally, for each profile, the radial distance of the first extremum (minimum or maximum) from the center was determined (see Supplementary Figure 9). This value changes monotonically with the z-location of the particle and served for calibration. We repeated the calibration measurements on four different samples, measured on four different days and took the average. Subsequently, for each image in the experimental trajectories, the radial distance of the first extremum was determined analogously and the corresponding z-position determined according to the calibration curve.

Extracting and characterizing the 3D potential

From the extensive sampling of the particle's position (~10^6 to 10^8 positions per recording), a detailed spatial probability density, $P_{3D}(r)$, can be obtained and related to the corresponding potential, $G(\boldsymbol{r})$, as a function of particle position according to

$$G_{3D}(r) = -k_B T \ln P_{3D}(r)\,, \tag{1}$$

where $\boldsymbol{r}$ is the position vector of the particle, k_B is the Boltzmann constant, and T = 295 K is the temperature. To determine the potential, only data points with a z-position between 10.5 and 11.7 µm were used, where precise axial localization was possible (Supplementary Figures 8 and 9). Typically, less than 0.3% of the data points were outside this range and had to be discarded. Discarding these data points mainly influenced the resolution of the energy landscape at the top of the barrier, since the particle mainly travels outside the specified z-range when it is not stably trapped in one of the minima, and did not influence the transition paths and hence transition path times (see Supplementary Figure 10).

The shapes of the resulting free-energy barrier and the potential wells of the potential of mean force projected on the x-axis, $G_{1D}(x) = -k_B T \ln P_{1D}(x)$, can be approximated by a harmonic function, $G_{1D}(x) = 0.5\,\kappa x^2$, where κ is the curvature. To estimate the uncertainties in the curvatures, the potentials were fitted over three different ranges in energy (depending on the barrier height ranging from 0.25 to 3.0 $k_B T$), from which we determined the means and standard deviations of the curvatures. Most potentials were slightly asymmetric, resulting in different barrier heights for transitions starting from the left and right wells, respectively. For determining rate coefficients as a function of barrier height, dwell times for transitions in both directions were analyzed separately. For

the analysis of mean transition path times and transition path time distributions, the barrier heights for transitions starting from both wells were averaged, and the resulting standard deviation used as the uncertainty in the height.

Transition rates and comparison to Kramers theory

The results presented Fig.2 of the main text were obtained from 24 recorded trajectories of different particles and/or laser powers, with a total of 7637 transitions.

Dwell time analysis was performed along the x-axis. To extract the dwell times and corresponding transition rates, the time traces were down-sampled from 30 kHz to 500 Hz by averaging the coordinates to reduce analysis time. To eliminate the influence of noise in the x-coordinate, which can lead to apparent transitions and shorten the resulting dwell times, we chose the threshold not half-way between the wells (as is used in standard thresholding methods), but at 75% of the distance between the wells relative to the starting well. To extract the transition rate coefficient, *k*, the survival probability, as a function of time *t*, was fitted with a single-exponential decay, e^{-kt}. These experimentally determined transition rates were compared with the transition rates for an overdamped Brownian particle in a potential as predicted by Kramers theory according to

$$k = k_0 e^{-\Delta G^{\ddagger}/k_B T}, \tag{2}$$

where $\Delta G^{\ddagger}$ is the barrier height in the potential of mean force projected on the x-axis, and k_0 the pre-exponential factor given by

$$k_0 = \frac{D}{2\pi k_B T}\sqrt{\kappa_b \kappa_w}, \tag{3}$$

where *D* is the translational diffusion coefficient of the particle, and κ_b and κ_w are, respectively, the curvatures of the potential of mean force at the top of the barrier and at the bottom of the potential well. We note that the projected dynamics along more general one-dimensional coordinates may involve non-Markovian, memory effects – in such cases, Langer's multidimensional model can be mapped [3,4] onto the one-dimensional Grote-Hynes theory [5], which is a generalization of Kramers theory that accounts for memory. Due to the decoupling of the dynamics along *x* near the barrier, however, these dynamics remain Markovian, and the Kramers description is adequate in our case. (This conclusion is further supported by the analysis presented in Figure 5, which shows that the dynamics is, indeed, Markovian and can be described by a one-dimensional Langevin equation.)

The mean-squared-displacement (MSD) of the particle in the x-coordinate was calculated according to (Supplementary Figure 3)

$$MSD = \frac{1}{N}\sum_{n=1}^{N}\big(x_n(t) - x_n(0)\big)^2. \tag{4}$$

D was extracted from the MSD at times up to 165 μs, a range where the optical trap does not influence the motion of particle, using

$$MSD = 2Dt + c, \tag{5}$$

where *c* is the intercept of the MSD at $t = 0$, which is the result of the residual experimental uncertainty in the particle position. We found diffusion coefficients in the range of 0.73 – 0.89 $\mu m^2\ s^{-1}$. The expected diffusion coefficient for a microsphere with a radius of 270 nm is 0.80 $\mu m^2\ s^{-1}$ according to the Stokes-Einstein relation, corresponding to the expected particle-to-particle variation in radius of $\pm$10 - 15% specified by the supplier. Diffusion coefficients from the MSD at short times agreed with the diffusion coefficients obtained from the diffusive component of the position correlation function (Figure 1c) according to $D = k_B T/\tau_r k$, where τ_r is the observed relaxation time and *k* the spring constant of the potential well.

Identifying transition paths

Transition path analysis was performed using a custom-written routine (Wolfram Mathematica 11). The boundaries for the start and end of transition paths were chosen half way between the energy top of the barrier and minimum of the well based on an interpolation of the measured 3D energy landscape (using the Mathematica function *ListInterpolation*, with method spline and order 3). The start of a transition trajectory was defined as the first data point with an energy greater than the initial boundary, while the end of the transition trajectory was the first data point with an energy less than the final boundary. The transition trajectory was only identified as a transition path if the start and end points were in different potential wells. From the set of transition paths obtained for each individual particle, only the transitions for which more than 80% of the data points had a z-position within 10.5 and 11.7 μm were used to determine averages and distributions of transition path times. This procedure eliminated artificial rapid transitions (less than ~1 ms, caused by a lack of contrast of the images outside this range and resulting in unreliable particle positions), whereas the rest of the transition path distributions was virtually unaffected (Supplementary Figures 10 and 11).

To validate our experimental methodology of identifying transition paths in the experimental data, we performed 3D-Brownian dynamics simulations of a particle on the interpolated energy landscapes with the experimentally determined diffusion coefficients and generated time traces of similar length as in the experiments. The simulations were performed with time-steps equivalent to a frame rate of 250 kHz to also be able to test whether the experimental frame rate of 30 kHz was sufficient for accurately identifying transition paths. Moreover, normal distributed noise was added to the simulated time traces; its standard deviation (7 nm) was chosen so that the intercept in the resulting mean-squared-displacement was similar to the one found experimentally (see Eq. 5). The resulting time traces were analyzed in the same way as the experimental data and compared to the experimental results in terms of barrier heights, transition rates, average transition path times, and transition path time distributions (Supplementary Figure 12).

Vertical error bars in Fig.3 of the main text result from the uncertainties in the curvatures of the barrier, the diffusion coefficient, and the TP time, obtained by bootstrapping. Horizontal error bars result from the difference in barrier heights for transitions starting in the left and right well, respectively.

Estimating the friction memory kernel $\xi(t)$ from experimental trajectories

Assuming that the dynamics are governed by an overdamped generalized Langevin equation of the form

$$0 = -G'_{1D}(x) - \int_{-\infty}^{t} \xi(t-t')\dot{x}(t')dt' + \zeta(t)\,, \tag{6}$$

where $\zeta(t)$ is a Gaussian-distributed random force with zero mean that satisfies the fluctuation-dissipation theorem, $\langle \zeta(t)\zeta(t') \rangle = k_B T \xi(t-t')$, we estimated the friction memory kernel using the exact formula [6]:

$$\hat{\xi}(s) = \hat{C}_{fx}(s)\left[s\hat{C}_{xx}(s) - C_{xx}(0) \right]^{-1}. \tag{7}$$

Here, $\hat{\xi}(s) = \int_0^\infty \xi(t) e^{-st} dt$ is the Laplace transform of the memory kernel, and $\hat{C}_{xx}(t)$ and $\hat{C}_{fx}(t)$ are the Laplace transforms of the position-position and force-position correlation functions, $C_{xx}(t) = \langle x(t)x(0) \rangle$ and $C_{fx}(t) = \langle -G'_{1D}[x(t)]x(0) \rangle$, respectively. The memory kernel is reported in Laplace space in Figure 5.

Estimating the average shape and velocity of transition paths.

The effective velocity of transition paths at point *x*, $v_{TP}(x)$, is defined [7] as the ratio of the length of a short interval, Δx, centered at *x* and the mean cumulative time spent by transition paths in this interval. It was estimated using the formula [7]

$$\frac{1}{v_{TP}(x)} = \langle \tau_{TP} \rangle P(x \mid TP), \tag{8}$$

where $P(x \mid TP)$ is the probability density of visiting point *x*, given that the system is on a transition path. The velocity profile was computed directly using Eq. 8. It was also compared to the exact analytical formula valid in the case of diffusive dynamics with a constant diffusion coefficient, *D*, [7]

$$\frac{1}{v_{TP}(x)} = \left(\int_{x_1}^{x_2} \frac{dx'}{DP_{eq}(x')} \right) \Phi_1(x)\Phi_2(x)P_{eq}(x), \tag{9}$$

where $P_{eq}(x)$ is the equilibrium distribution of the reaction coordinate, *x*, and $\Phi_{1(2)}(x) = 1 - \Phi_{2(1)}(x)$ is the splitting probability, i.e., the probability, having started from *x*, to reach the boundary x_1 (x_2) before the boundary x_2 (x_1). The splitting probability is given by

$$\Phi_1(x) = 1 - \Phi_2(x) = \int_{x_1}^{x} P_{eq}^{-1}(x')dx' \Big/ \int_{x_1}^{x_2} P_{eq}^{-1}(x')dx'. \tag{10}$$

We note that by taking the time derivative of the average transition path, $\tilde{v}_{TP} = dx_{TP}(t)/dt$, one obtains an alternative definition of the transition path velocity. [8]

We have also estimated the average shape of the transition path, $x_{TP}(t)$, which is defined [9] through the inversion of the dependence of the average times, $\langle t_{first}(x_{TP}) \rangle$ and $\langle t_{last}(x_{TP}) \rangle$, that a transition path from x_1 to x_2 takes to cross a point x_{TP} for the first time and for the last time before arriving at the boundary x_2. Since this definition leads to a path that is not time-reversible, we have also estimated the symmetrized average path shape [30,32] defined via inversion of the coordinate dependence of the symmetrized average time

$$\langle t_{sym}(x) \rangle = \frac{\langle t_{first}(x) \rangle + \langle t_{last}(x) \rangle}{2}. \tag{11}$$

For diffusive dynamics, exact analytical expressions exist for these shapes, which are compared with the experimental results in Fig. 5e. Specifically,

$$\left\langle t_{first}(x)\right\rangle = \left\langle \tau_{TP}(x_1 \leftrightarrow x)\right\rangle \tag{12}$$

and

$$\left\langle t_{last}(x)\right\rangle = \left\langle \tau_{TP}(x_1 \leftrightarrow x_2)\right\rangle - \left\langle \tau_{TP}(x \leftrightarrow x_2)\right\rangle, \tag{13}$$

where $\left\langle \tau_{TP}(x_1 \leftrightarrow x_2)\right\rangle$ is the mean transition path time between the boundaries x_1 and x_2 (and similar definitions, with boundaries changed accordingly, are used in Eqs. 12, 13), given by the analytical expression [10]:

$$\left\langle \tau_{TP}(x_1 \leftrightarrow x_2)\right\rangle = \left(\int_{x_1}^{x_2} \frac{dx'}{DP_{eq}(x')}\right) \int_{x_1}^{x_2} \Phi_1(x)\Phi_2(x)P_{eq}(x)dx \cdot \tag{14}$$

The most probable transition path from x = -*L* to *L* using the harmonic approximation was calculated according to [8]:

$$\left\langle x\left(t \mid \tau_{TP}\right)\right\rangle = \frac{L\sinh\left(\kappa D/k_B T\left(t-\tau_{TP}/2\right)\right)}{\sinh\left(\kappa D/k_B T\left(\tau_{TP}/2\right)\right)}. \tag{15}$$

Deviations between experimental data and theoretical curves in Fig. 5e were quantified in terms of summed squared deviations, yielding $2.74\cdot10^{-3}$ for the average first crossing time (red line in figure), $4.62\cdot10^{-3}$ for the average last crossing time (blue line in figure), $2.84\cdot10^{-3}$ for the average TP shape (gray line in figure), and $0.27\cdot10^{-3}$ for the most probable TP (dashed black line in figure).

References

[1] R. Parthasarathy, Rapid, accurate particle tracking by calculation of radial symmetry centers. Nat. Methods **9**, 724 (2012).

[2] A. Jain, A. H. Yang, and D. Erickson, Gel-based optical waveguides with live cell encapsulation and integrated microfluidics. Opt. Lett. **37**, 1472 (2012).

[3] A. Berezhkovskii and A. Szabo, One-dimensional reaction coordinates for diffusive activated rate processes in many dimensions. J. Chem. Phys. **122**, 14503 (2005).

[4] D. E. Makarov, Interplay of non-Markov and internal friction effects in the barrier crossing kinetics of unfolded proteins. J. Chem. Phys. **138**, 014102 (2013).

[5] R. F. Grote and J. T. Hynes, The stable states picture of chemical reactions. II. Rate constants for condensed and gas phase reaction models. J. Chem. Phys. **73**, 2715 (1980).

[6] R. Satija and D. E. Makarov, Generalized Langevin Equation as a Model for Barrier Crossing Dynamics in Biomolecular Folding. J. Phys. Chem. B **123**, 802 (2019).

[7] A. M. Berezhkovskii and D. E. Makarov, Communication: Transition-path velocity as an experimental measure of barrier crossing dynamics. J. Chem. Phys. **148**, 201102 (2018).

[8] P. Cossio, G. Hummer, and A. Szabo, Transition paths in single-molecule force spectroscopy. J. Chem. Phys. **148**, 123309 (2018).

[9] W. K. Kim and R. R. Netz, The mean shape of transition and first-passage paths. J. Chem. Phys. **143**, 224108 (2015).

[10] G. Hummer, From transition paths to transition states and rate coefficients. J. Chem. Phys. **120**, 516 (2004).

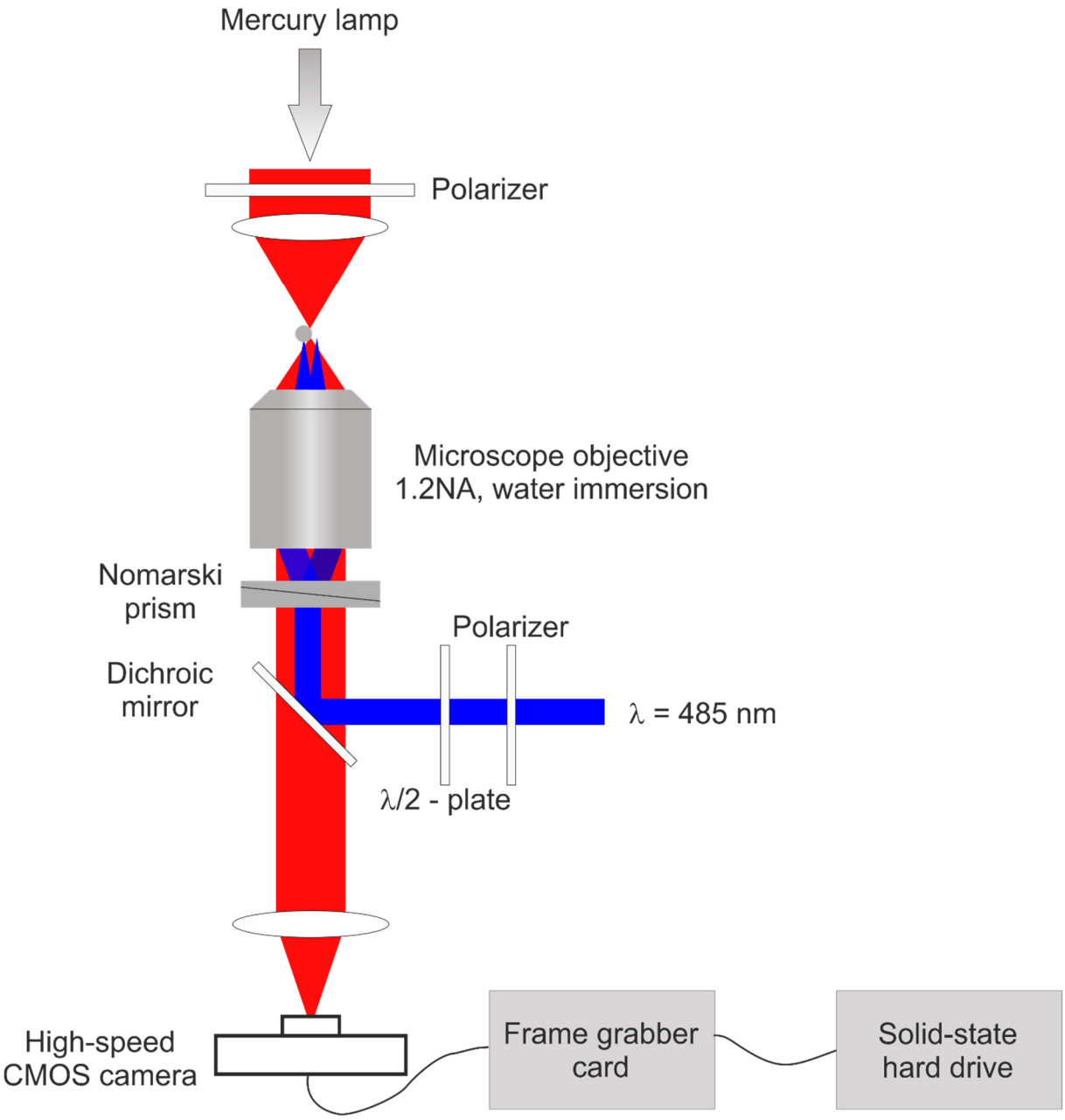

Figure S1: Experimental setup. A linearly polarized laser beam is focused by a microscope objective after passing through a Nomarski prism, which splits the light into two orthogonally polarized beams, leading to two optical traps with a stable displacement of ~400 nm in the focal plane of the high-aperture microscope objective. The relative stiffnesses of the traps are adjustable by rotating the lambda-half plate. The particle position is imaged onto a high-speed CMOS camera using Köhler illumination with the light of a mercury vapor lamp. A fast frame grabber card stores the images on a solid-state drive.

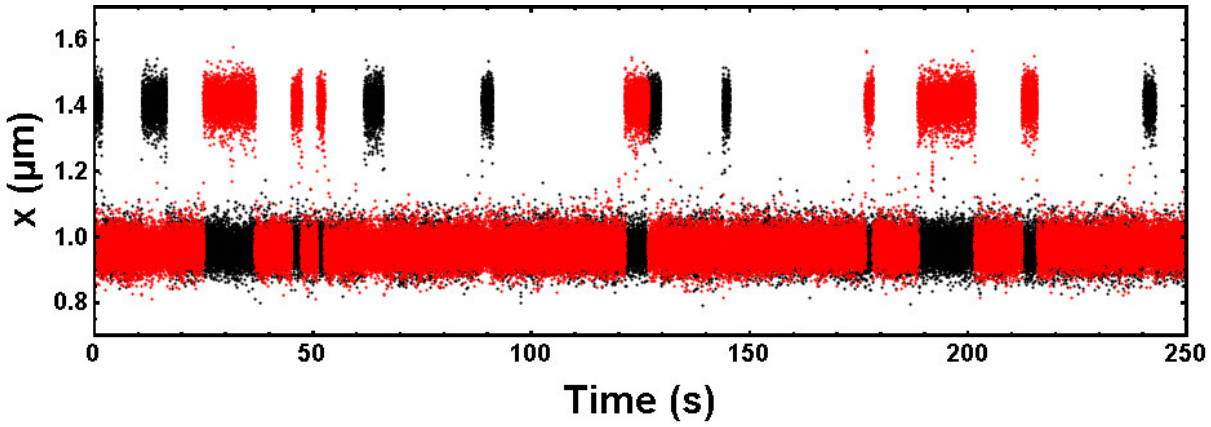

Figure S2: Long-term stability of the experimental setup demonstrated by the superposition of the first and last 250 seconds (black and red) of a 3300 s long time trace of the bead's x-position. No instrument drift is visible over this time span.

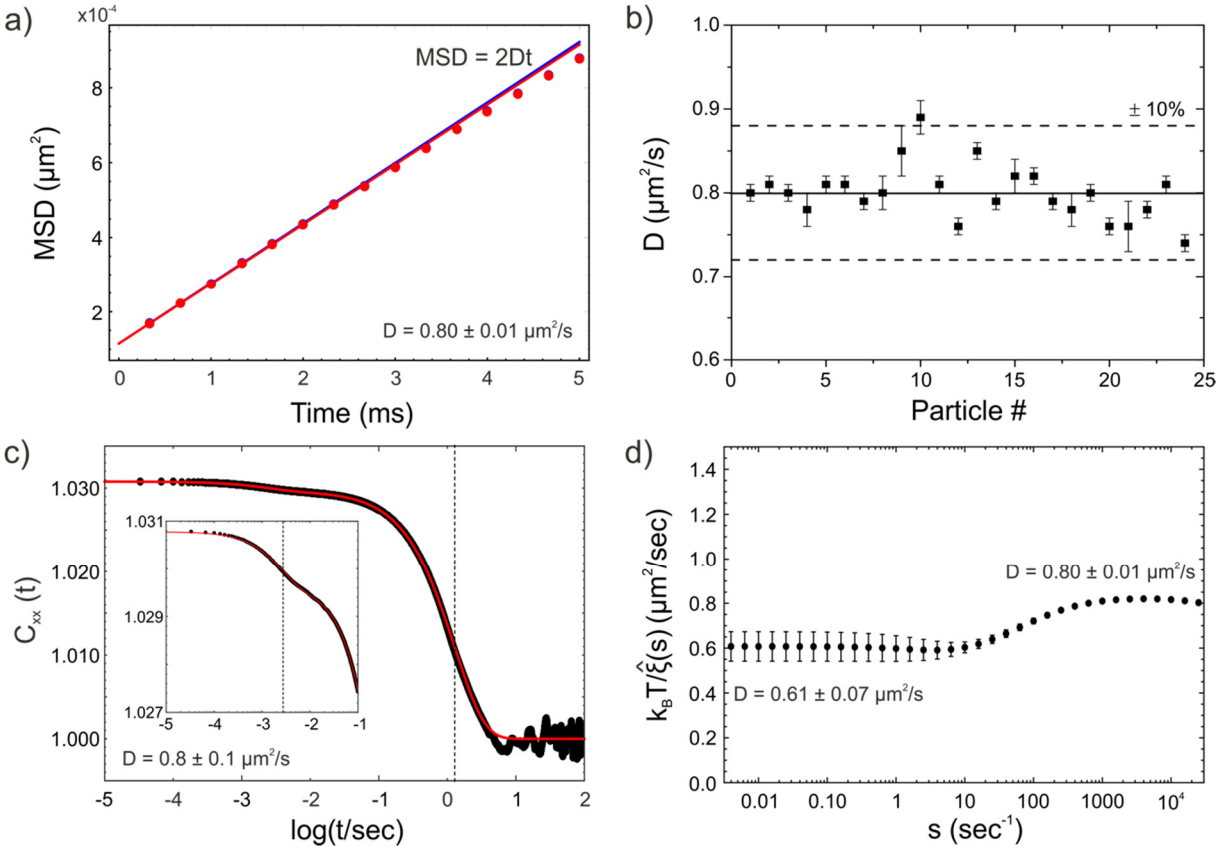

Figure S3: Quantifying translational diffusion coefficients. a) For each particle, the diffusion coefficient is determined from its mean-squared displacement (MSD) in the potential wells at short times (see Methods). The red and blue data points are examples obtained from the particle residing in the left and right well, respectively. The offset in the MSD at time zero is a result of the uncorrelated uncertainty in the particle's position due to noise in the images. **b)** The diffusion coefficients for all particles were within the 10-15% deviation from the mean value, which matches the diffusion coefficient expected for a sphere with a radius of 270 nm, as determined via the Stokes-Einstein equation, in accord with the supplier's specifications. **c)** The position autocorrelation function, C_{xx}, of a particle in the bistable optical trap shows components corresponding to the diffusive dynamics within each trap (relaxation time of 2.7 ± 0.1 ms in this example, corresponding to a diffusion coefficient of 0.8 ± 0.1 μm^2/s, see inset with zoom) and to the kinetics of transitions between them (relaxation time of 1.3 ± 0.1 s in this example, in agreement with the inverse sum of the transition rate coefficients, 1.1 ± 0.3 s). **d)** The estimate of the diffusion coefficient based on the friction coefficient from the memory kernel at high frequency, where the error is smallest, and the Einstein relation, $D = k_B T / \xi_0$, yields 0.80 ± 0.01 μm^2/s, in agreement with the value from the mean square displacement (0.80 ± 0.01 μm^2/s) and the position correlation function (0.9 ± 0.1 μm^2/s).

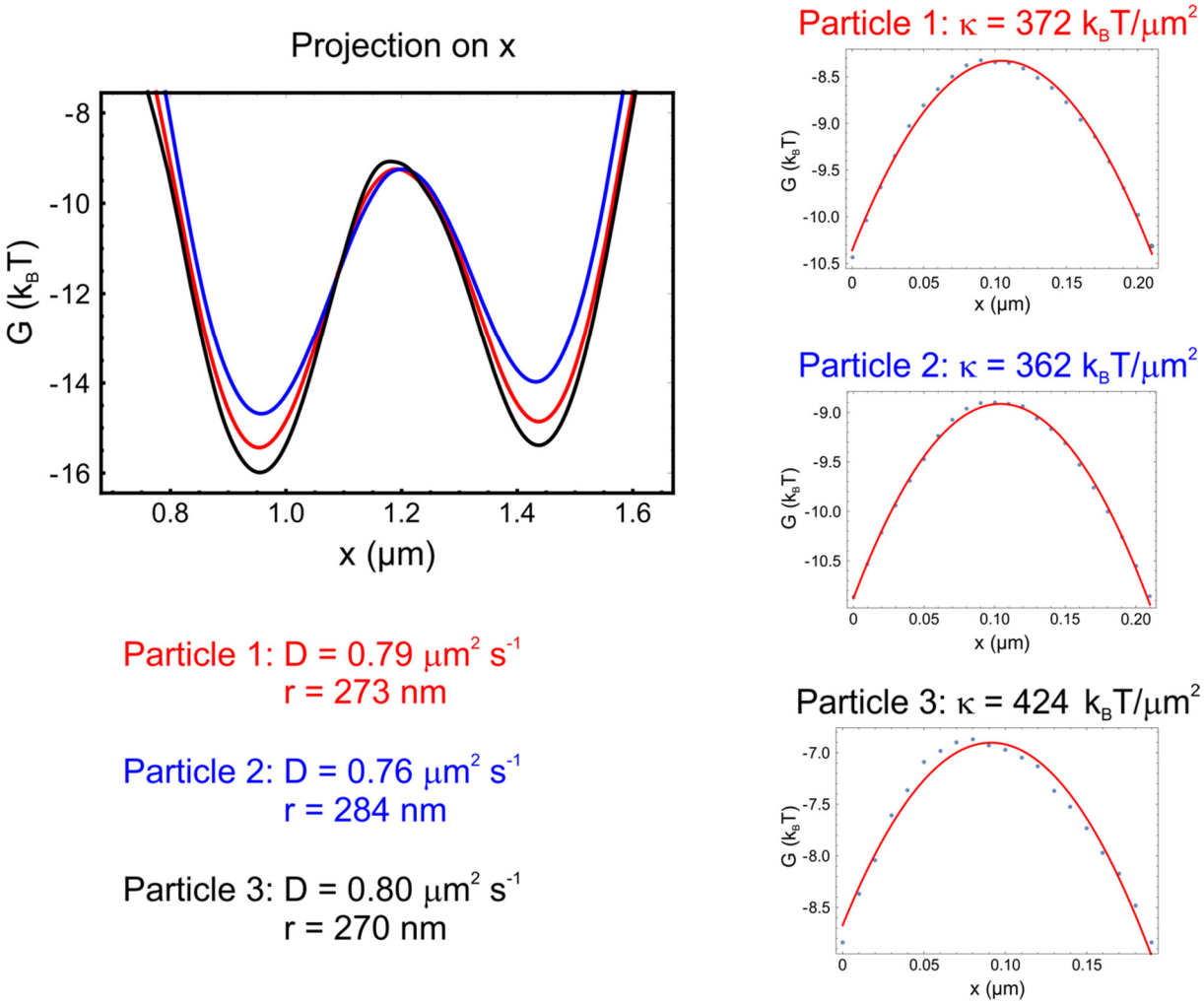

Figure S4: Particle-to-particle variability leads to measurable differences in the trapping potential. Potentials of mean force extracted for three particles with slightly different radii but at identical laser power. For each particle, the shape of the potential of mean force is measurably different, with pronounced differences in well depth/barrier height (left side) and slight differences in the curvature at the top of the barrier (right side).

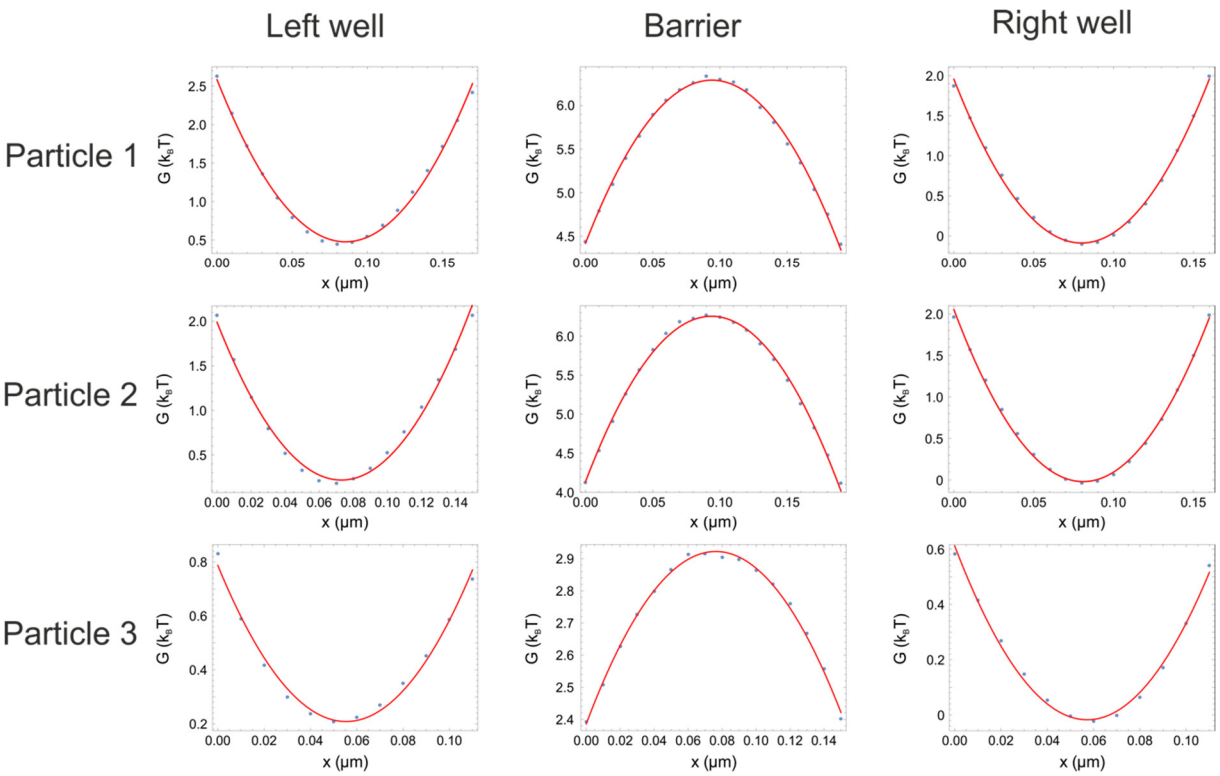

Figure S5: Analysis of curvatures. Examples of curvatures from fits of the energy barriers and wells of the potentials of mean force of three different particles at three different laser powers. Each curve was fitted over three different ranges of energies between 0.5 and 3 $k_B T$ relative to the top of the barrier or bottom of the well. The means and standard deviations of the extracted curvatures were used for the further analysis in terms of Kramers theory or barrier crossing.

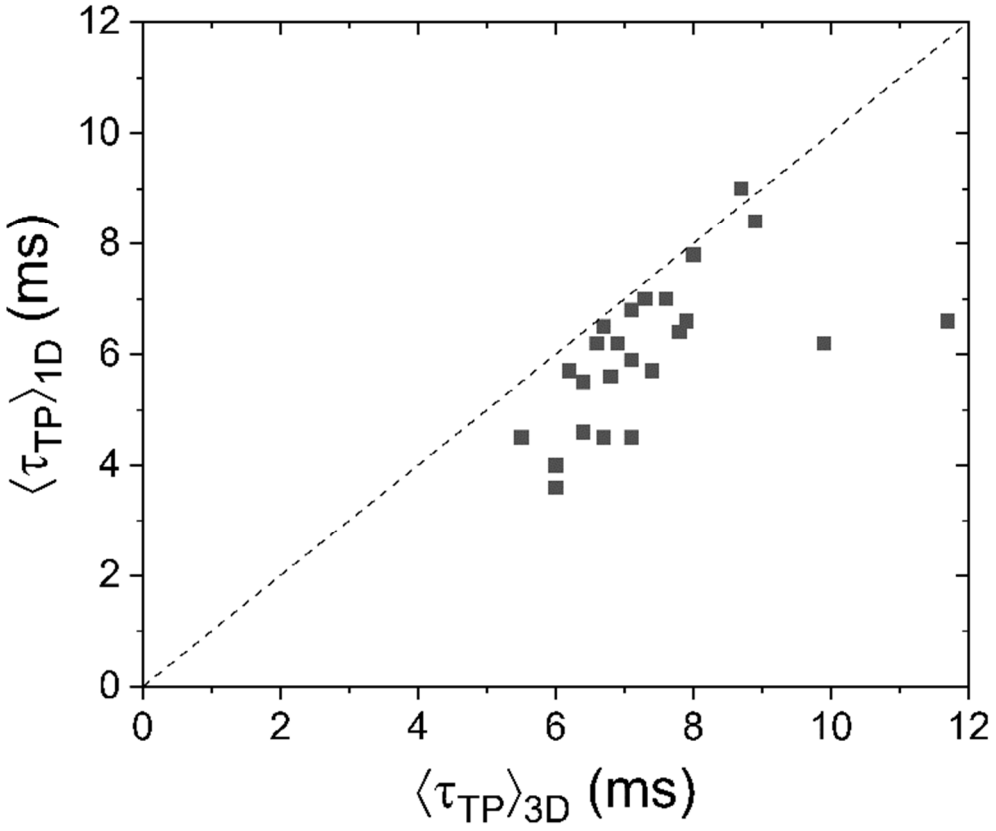

Figure S6: Comparison of mean transition path times obtained from 1D- and 3D-analysises of the experimental data. Transitions path times extracted from the 1D trajectories along the x-coordinate are on average ~15% shorter than the ones extracted from the 3D trajectories owing to the different choice of transition path boundaries in the two types of analysis.

$\Delta G^* = < 2\ k_B T$

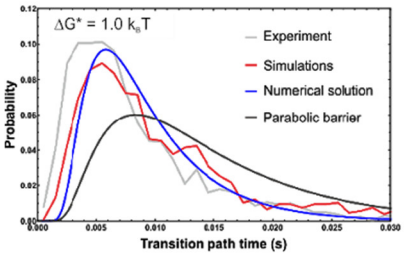

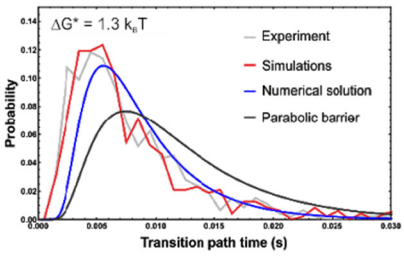

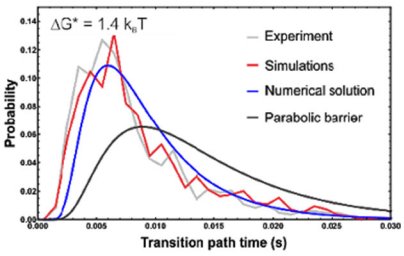

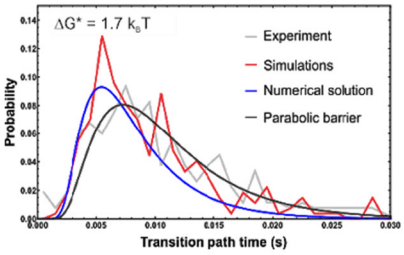

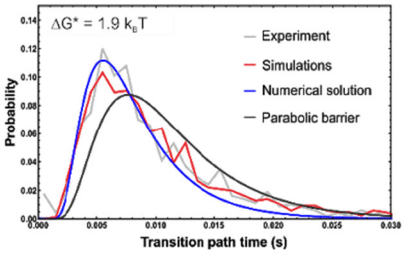

$\Delta G^* = 2 - 3\ k_B T$

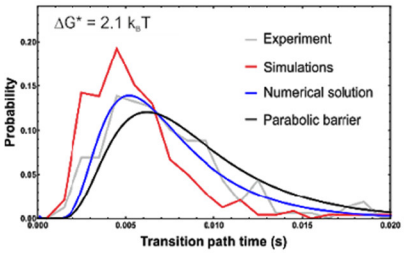

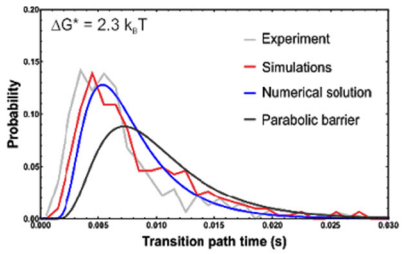

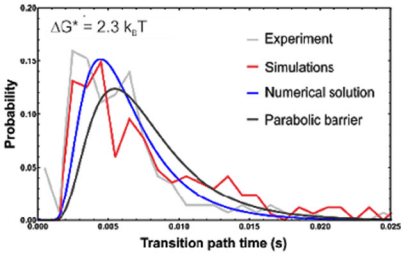

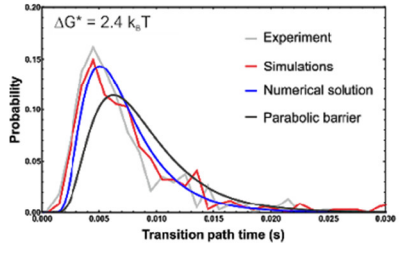

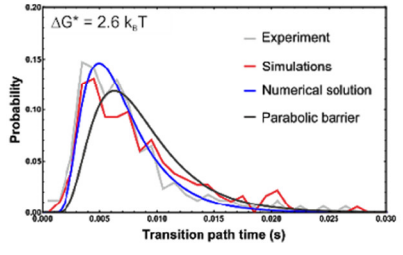

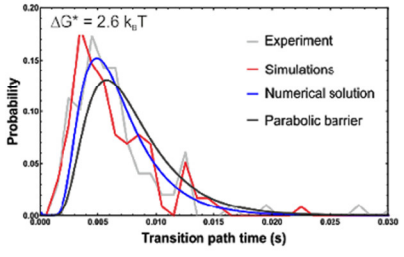

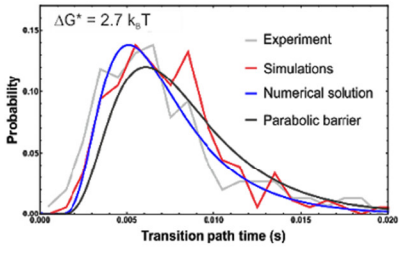

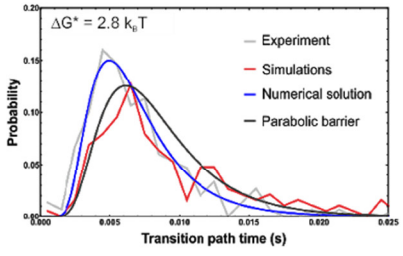

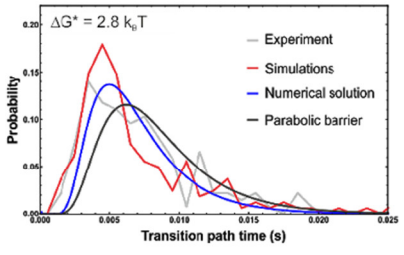

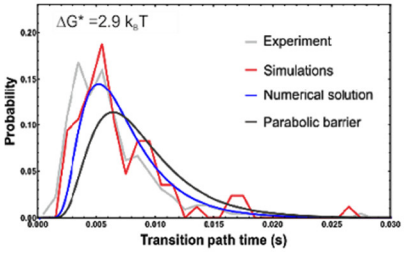

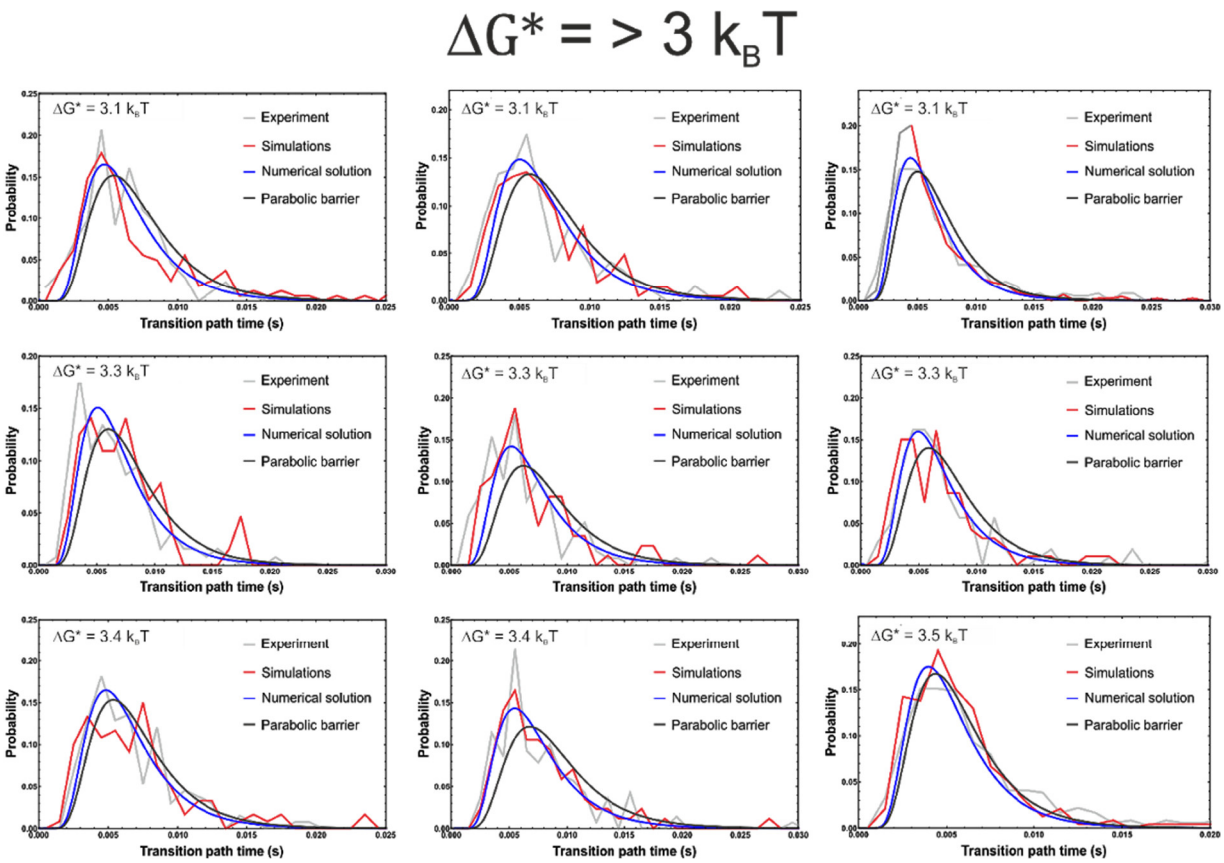

Figure S7: Transition path time distributions. Distributions of transition path times obtained from the 3D trajectories of each individual particle sorted by Δ*G**, where ΔG* is the average of the two barrier heights relative to the left and right well. Each experimentally obtained distribution (gray) is compared to the distribution obtained from Brownian dynamics simulations (red), the numerical solution of the diffusion problem (blue), and the parabolic barrier approach (black, Szabo equation). Since the durations of the simulated trajectories (and therefore the total number of transitions therein) were chosen to be similar to the experimental ones, the noise in the distributions from the simulated and experimental data is also similar.

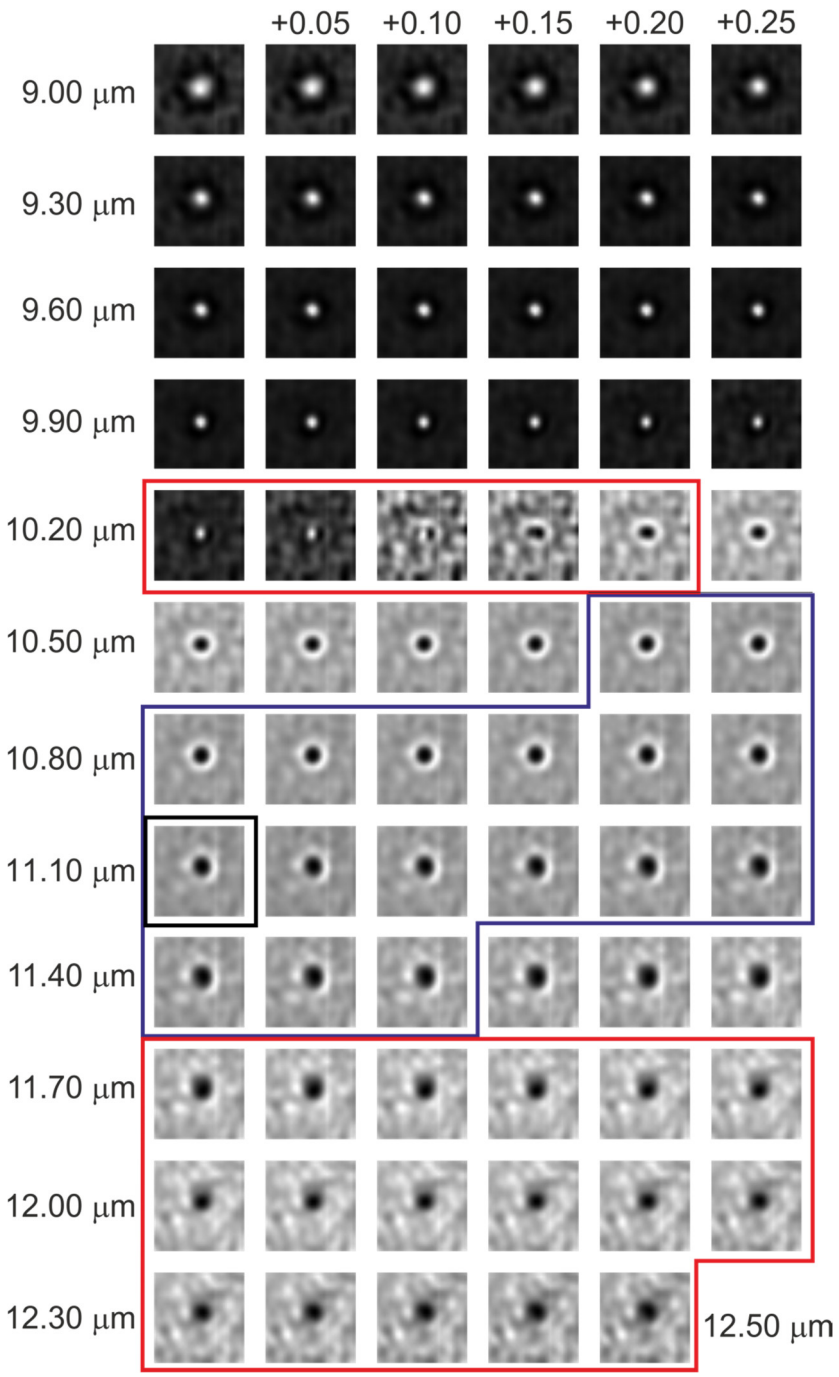

Figure S8: Calibration of z position. A calibration stack of images is generated from particles embedded and thus immobilized in a 2% agarose gel. Each image in the stack is the average of 10,000 images recorded at 30-kHz frame rate. The z-position was adjusted in 50-nm increments. The blue line indicates the most occupied range of z positions when the particles are trapped; the image framed in black shows the typical center position. The red lines indicate where determining the position of the particle is problematic due to a lack of contrast. The number on the left indicates the z position for the left-most image.

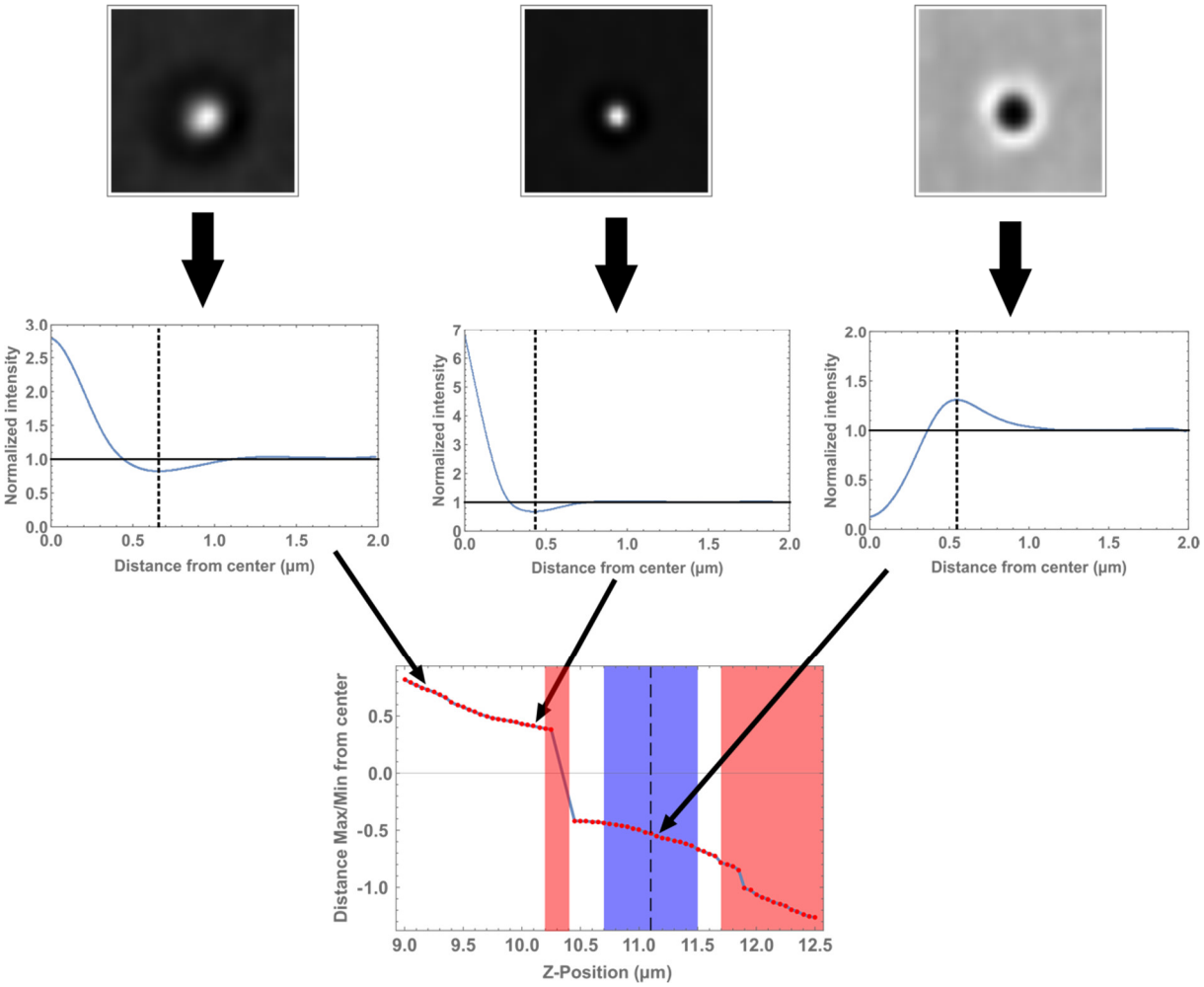

Figure S9 Determining the particle position in z. For each image from the calibration stack (see Supplementary Figure S8 for a full stack), the center of the particle is determined using the radial symmetry of the diffraction pattern. We obtain a radial intensity profile, $I(r)$, by angular integration and normalizing to the signal far from the bead, such that $I(r \gg 0) = 1$. Next, the distance, r_z, between the center of symmetry and the first minimum or maximum is determined. Finally, we construct a calibration curve by taking $+r_z$ if $I(r = 0)$>1, and $-r_z$ if $I(0) \leq 1$. The calibration curve shown here is the average of four independent calibration stack recordings. The blue region indicates the most occupied z-range of a trapped particle, with the black dashed line being the average location of the particle. The red areas indicate ranges where the localization precision of the bead is reduced due to a lack of contrast (see Figure S8).

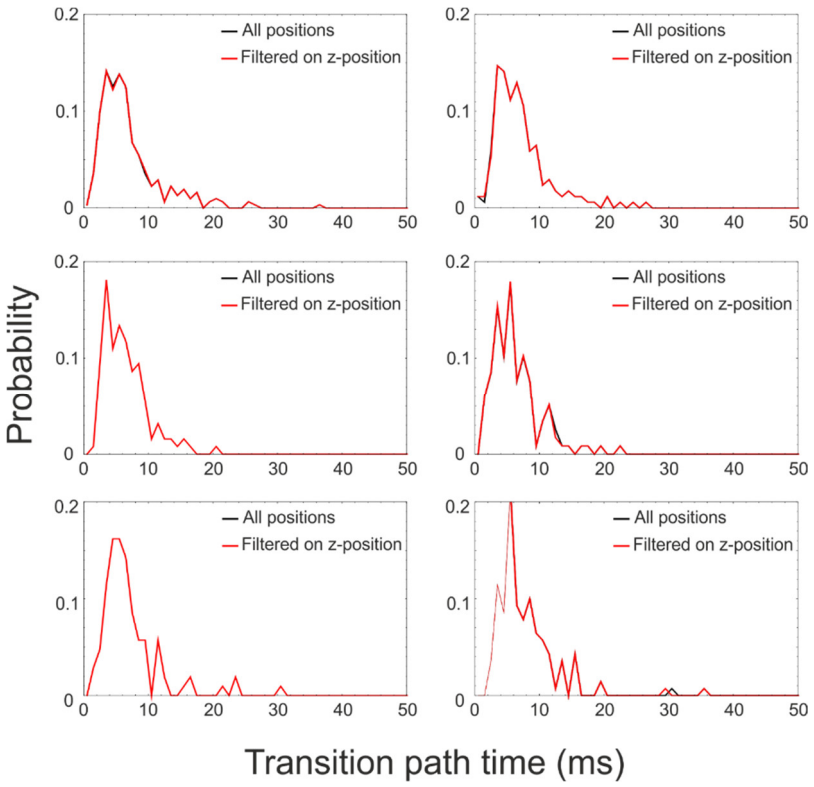

Figure S10: Robustness of the transition-path-time determination on the range of z-positions used for reconstructing the energy landscape. Comparison of the transition path time distributions based on all bead positions (black) with those using only the positions with z-values between 10.5 and 11.7 µm (red) shows no significant differences. For this comparison, simulated 3D-trajectories (Brownian motion on six of the experimentally determined energy landscapes) were analyzed.

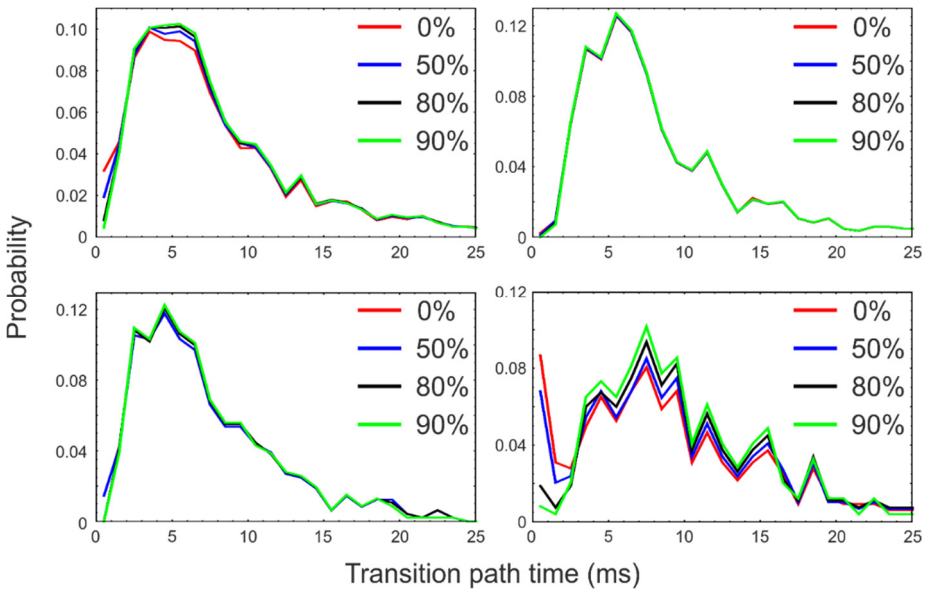

Figure S11: Measured transition path time distributions are robust to the range of z positions used. Effect of including only the transition paths for which more than a given percentage of the data points have a z-position between 10.5 and 11.7 µm, illustrated for four different representative data sets. As the distributions show, an increasing percentage mainly excludes very fast apparent transitions with a duration of less than 1 ms owing to a lack of precise position information, most of which are eliminated with a threshold of 80%. Increasing the percentage from 80% to 90% resulted in discarding some longer transitions for which we can still determine the transition path time accurately due to the large number of frames within the transitions.

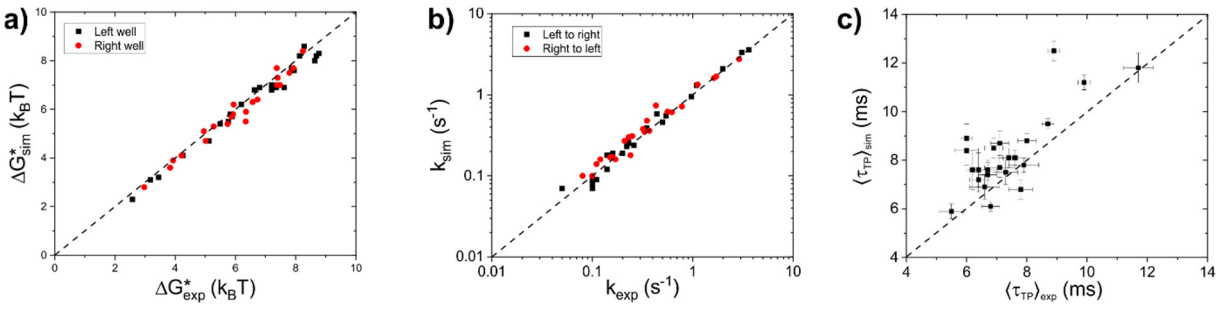

Figure S12: Comparison of 3D-Brownian dynamics simulations and experimental data. Experimentally obtained energy landscapes and diffusion coefficients were used for the simulations, which were then analyzed in the same way as the experimental data. **a)** The barrier heights extracted from experiment and simulation agree well. Red and black data points represent the barrier heights with respect to the left and right wells, respectively. The dashed curve marks the identity line. **b)** The transition rates between the wells, in the same representation as in **a**. **c)** The average transition path times obtained from experimental and simulated data. The error bars were obtained from bootstrapping. The remaining small differences in the average transition path times determined from experiment and simulations are the result of artificially rapid transitions in the experimental data that could not be fully eliminated. For a more detailed discussion, see *Identifying transition paths* in the Methods section of the Supplementary Information.